ACS Catalysis

pubs.acs.org/acscatalysis
Research Article

Active Site Evolution under Working Conditions in Fe–Co Dual-Atom Electrocatalyst

Elisabetta Inico,† Matteo Spotti,† Gianfranco Pacchioni,* and Giovanni Di Liberto*

Cite This: ACS Catal. 2026, 16, 9810–9822
Read Online

ABSTRACT: Single-site catalysis plays a central role in electrochemical applications, where the activity critically depends on the local coordination and dynamic evolution of the active sites under operating conditions. Using the FeCo–N_3O_3@C dual-atom catalyst (DAC) as a model system, we combined density functional theory calculations and microkinetic modeling to investigate its performance in the oxygen evolution (OER) and oxygen reduction (ORR) reactions and to demonstrate the importance of the evolution of the structure of the catalyst under working conditions. Our results reveal that while OER proceeds on the Co site of the as-prepared catalyst, the ORR occurs on a different, dynamically formed active site. Under reaction conditions, water dissociates to yield a stable Co–OH adduct that blocks the Co site for ORR, thereby shifting activity to the Fe center. This restructuring reconciles theory with experiment and explains the high bifunctional performance of FeCo–N_3O_3@C. The computed polarization curves accurately reproduce the experimental OER and ORR behavior, demonstrating the necessity of explicitly simulating electrochemical conditions rather than relying solely on static Gibbs free energy diagrams. Analysis of Co and Fe K-edge XANES spectra and Bader charge variations further supports the proposed mechanism. Overall, this study highlights the importance of considering the evolution of single- and dual-site catalysts under working conditions and the synergistic interaction between neighboring Fe and Co atoms. Such insights advance our understanding of dynamic catalytic behavior and provide guidance for the rational design of efficient SAC and DAC systems.

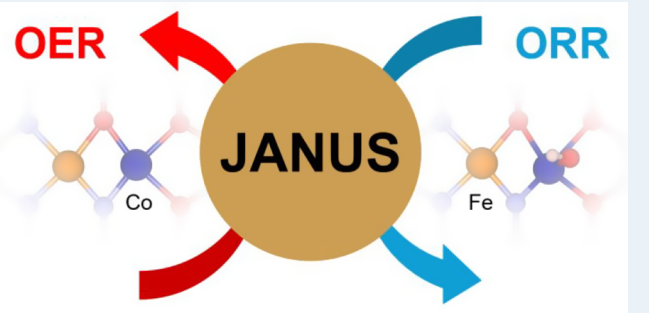

KEYWORDS: *single-atom catalyst, dual-atom catalyst, oxygen evolution reaction, oxygen reduction reaction, janus dual-atom catalyst*

1. INTRODUCTION

Determining the mechanism of a catalytic reaction remains a fundamental yet challenging task, as it provides the key to rationally improving the performance, selectivity, and stability of a given catalyst. Achieving this goal requires precise and comprehensive knowledge of the active site and its dynamic role during the reaction.[1−4] Over the past decades, substantial progress has been made in developing advanced experimental and computational techniques to characterize the structure, composition, and electronic properties of active sites in heterogeneous catalysts.

A particularly significant advancement in this field has emerged with the development of single-atom catalysts (SACs),[5−8] in which isolated transition-metal (TM) atoms are stabilized within a solid matrix.[9] These systems offer an ideal platform to bridge the gap between homogeneous and heterogeneous catalysis, owing to their uniform and atomically dispersed active centers.[10−12] The combination of state-of-the-art microscopy techniques, such as High-Angle Annular Dark-Field Scanning Transmission Electron Microscopy (HAADF-STEM) and Aberration-Corrected STEM, with complementary spectroscopic approaches, including X-ray Absorption Spectroscopy (XAS),[13,14] X-ray Photoelectron Spectroscopy (XPS), Electron Paramagnetic Resonance (EPR),[15] Infrared (IR) spectroscopy using probe molecules,[16] and solid-state Nuclear Magnetic Resonance (NMR) spectroscopy[17] enables the precise identification and characterization of such active sites.

Moreover, the interpretation of these experimental findings is often reinforced through first-principles calculations, which provide theoretical models that reproduce and rationalize the observed structural and electronic features.[6,18,19] The synergy between advanced characterization and computational modeling thus represents a powerful strategy for establishing a

Received: December 1, 2025
Revised: March 19, 2026
Accepted: April 28, 2026
Published: May 21, 2026

https://doi.org/10.1021/acscatal.5c08565
ACS Catal. 2026, 16, 9810–9822

detailed and reliable description of active sites,[20,21] an essential step toward elucidating catalytic mechanisms and guiding the design of more efficient catalysts.

Dual-atom catalysts (DACs) represent an emerging class of catalytic materials in which two metal atoms, either identical or different, are stabilized in close proximity on a support.[22−25] These paired metal centers can cooperate synergistically, enabling reaction pathways that are inaccessible to isolated SACs. The unique electronic and geometric interactions between the two atoms can modulate adsorption energies, facilitate multielectron transfer processes, and enhance both activity and selectivity. Depending on their composition and configuration, DACs can bridge the gap between single-atom and nanoparticle catalysts, offering a versatile platform for tuning catalytic performance at the atomic scale.[26−28]

Even subtle modifications in the local structure and coordination environment of a SAC or a DAC can lead to profound changes in their catalytic behavior. The electronic structure and reactivity of SACs and DACs are extremely sensitive to variations in coordination number, oxidation state, nature of the surrounding atoms or functional groups.[29,30] Small perturbations, such as the removal or addition of a neighboring atom, slight distortions in bond geometry, or changes in the metal–support interaction can alter the distribution of the metal's d-electron density, thereby modifying adsorption energies and reaction barriers.[31,32] Consequently, even nominally identical catalysts may exhibit markedly different activity or selectivity under different preparation methods or reaction conditions. This pronounced structure–reactivity sensitivity motivates the importance of precisely controlling the atomic environment in SACs and DACs.[33,34]

However, characterization of the active site in the *as-prepared* catalyst, while essential, often provides an incomplete picture of the catalytic process, as the catalyst structure can undergo significant modifications under reaction conditions. Variations in temperature, pressure, external potential and chemical environment can induce surface reconstruction, changes in oxidation state, poisoning by adsorbed species or the formation of new active phases.[16] Consequently, the nature, geometry, and electronic properties of the active sites present during catalysis may differ, sometimes substantially, from those observed in the pristine material.[35] These dynamic transformations imply that a comprehensive understanding of the reaction mechanism requires in situ or operando investigations capable of capturing the catalyst in its true working state.[36,37]

In general, dual-atom catalysts embedded in carbonaceous matrices exhibit synergistic interactions between neighboring metal centers, which modulate the electronic structure and charge distribution, thereby enhancing catalytic activity.[38] In the specific case of Fe–Co dual-atom catalysts, outstanding bifunctional activity toward both the oxygen reduction reaction (ORR) and oxygen evolution reaction (OER) in alkaline media has been reported, together with stability comparable to that of noble-metal catalysts.[39] Moreover, Fe–N_x and Co–N_x coordination motifs strongly interact with oxygenated intermediates (O_2*, OH*, and OOH*), effectively optimizing intermediate adsorption and reaction kinetics, which leads to significantly improved ORR performance.[40,41]

Recently, Tang et al. reported a synthetic strategy for constructing a carbon-based catalyst featuring diatomic Fe–Co sites, in which Fe and Co atoms are coordinated to N and O atoms, respectively, and interconnected through bridging N and O atoms (FeCo–N_3O_3@C).[42] The resulting FeCo–N_3O_3@C DAC exhibits remarkable stability and bifunctional catalytic activity toward both the oxygen reduction reaction (ORR) and the oxygen evolution reaction (OER). The work provided a comprehensive *ex situ* and in situ characterization, showing that the superior activity arises from the strong electronic coupling between the Fe–N_3 and Co–O_3 moieties. In particular, this interaction modulates the *d*-orbital energy levels of the metal centers, thereby optimizing the adsorption–desorption behavior of oxygenated intermediates and accelerating the reaction kinetics of both ORR and OER.

The proposed mechanism, which is predominantly based on X-ray Absorption Near Edge Structure (XANES) Spectroscopy, implies that the two atoms, Fe and Co, act separately, with Co promoting the OER, and Fe the ORR.[42] In addition density functional theory (DFT) calculations were performed based on the working hypothesis that the structural and electronic features of the active site in the as-prepared catalyst are preserved under reaction conditions. Although this assumption appears to be valid at first glance, certain aspects are incompatible with the thermodynamics of the process unless factors not accounted for in the original mechanism are involved. In particular, the origin of the preferential occurrence of the direct reaction (OER) and its reverse counterpart (ORR), which share the same reaction intermediates but take place on different sites, remains elusive, unless, for some reason, the nature of one of the two sites changes during the process. From a thermodynamic point of view, the reaction will always take place on the most active site available, both for the forward and the reverse reaction.

In this work, we have revisited the reaction mechanisms of the OER and ORR over the FeCo–N_3O_3@C DAC, incorporating new relevant terms and aspects in the mechanistic description,[20,43] such as the formation of all possible reaction intermediates[44] and the role of water as a coordinating ligand that in the course of the reaction forms reactive species that modify the nature of the active site.[45−47] By integrating these considerations, we unravel the origin of the reaction mechanism, that underscores a fundamental aspect of single-atom and dual-atom catalysis: the evolution of the active site under reaction conditions, leading to the formation of new species that significantly influence the reaction pathway. The provided mechanistic explanation in this work is compatible with the bifunctional activity of the catalyst, where the two OER and ORR reactions occur on two different sites, available and generated in reaction conditions.

Moreover, we demonstrate that conventional analyses based solely on the thermodynamic barriers for intermediate formation can be insufficient to predict catalytic performance. To reliably connect theoretical predictions with experimental observations, the calculation of polarization curves through microkinetic modeling must be integrated with the classical determination of the reaction profile.

These findings carry broader implications beyond the FeCo–N_3O_3@C system, which is considered here just as an exemplificative test system, providing general insights for the accurate description of activity in SACs, DACs, and heterogeneous catalysts more broadly. While our work is motivated by the compelling experimental evidence of the structure and activity of the DAC proposed by Tang et al., the conclusions extend beyond this specific system, offering guidelines for the rational evaluation and design of advanced catalysts.

https://doi.org/10.1021/acscatal.5c08565
ACS Catal. 2026, 16, 9810−9822

2. MODELING ASPECTS

2.1. DFT Approach

We performed spin-polarized density functional theory (DFT) calculations as implemented in the *Vienna Ab-initio* Simulation package (VASP).[48−50] The Perdew-Burke-Ernzherof (PBE) exchange and correlation functional was adopted.[51] The following valence electrons were treated explicitly: H (1s), C (2s,2p), N (2s, 2p), O (2s, 2p), Fe (4s, 3d), Co (4s, 3d). They have been expanded on a set of plane waves with a kinetic energy cutoff of 400 eV, while the core electrons were treated with the projector augmented wave approach (PAW).[52,53] The threshold criteria for electronic and geometry loops were set to 10^{-5} eV and 10^{-2} eV/Å, respectively. A 2 × 2 × 1 Monkhorst−Pack k-point grid[54] was used to sample the reciprocal space. The Grimme's D3 parametrization scheme was adopted to account for dispersion interactions.[55] Geometry optimizations were performed by means of the conjugate gradient algorithm. To accurately capture the magnetic character of Fe and Co centers, single-point PBE0[56,57] energy calculations were performed on PBE-optimized geometries to refine the electronic structure. This step is essential, as the adsorption energies of species interacting with transition-metal atoms having unpaired electrons in the ground state are particularly sensitive to the self-interaction error inherent in conventional DFT formulations.[58−60] We report a comparison of PBE and PBE0 energies in the ESI Section S1, showing that in some cases substantial differences exist between the two treatments. On the other hand, the general conclusions of this study are independent of the exchange-correlation functional used.

2.2. Structural Model

As mentioned earlier, the local coordination of the active phase plays a crucial role, as it is essential to accurately determine the nature and geometry of the ligands surrounding the metal atoms.[61−63] In the selected DAC model system, the active phase consists of an Fe atom located in close proximity to a Co atom, both embedded within a carbon matrix (Figure S1). This model was employed to investigate the OER and ORR. The starting point was a fully optimized graphene nanosheet, from which a $p(8 \times 8)$ supercell containing 128 atoms was constructed (lattice parameters: $a = b = 19.74$ Å and $\gamma = 120°$) to ensure sufficient separation between active sites. A defect was then introduced into the host matrix to accommodate the metal atoms, with the nearest-neighbour carbon atoms substituted by nitrogen and oxygen atoms, following the structural details reported in Ref. 42 (see Figure S1 and Table S1 for the calculated interatomic distances and Section S5 for Cartesian coordinates). Then, coordinates of the atoms have been re-optimized.

OER and ORR intermediates were modelled by using the Computational Hydrogen Electrode (CHE) approach.[64,65] In a series of pioneering works, it was demonstrated that a complex process such as an electrochemical reaction can be effectively modeled using quantum chemical calculations of reaction intermediates, through the construction of Gibbs free energy diagrams. Despite its inherent approximations, the CHE method has proven extremely successful and, most importantly, has provided valuable atomistic insights into a wide range of electrochemical reactions.[66−71] The Gibbs free energy of a species x can be calculated by adding to the DFT energies (ΔE_x) the entropic ($T\Delta S_x$) and zero-point energy ($\Delta E_{ZPE,\,x}$) contributions.

$$\Delta G_x = \Delta E_x - T\Delta S_x + \Delta E_{\mathrm{ZPE},x}$$

$\Delta E_{ZPE,\,x}$ can be estimated within the harmonic approximation. Here we allowed to vibrate the TM atoms of the active site and those of the intermediates. Entropies of gas-phase species can be taken from International Tables or calculated ab-initio with the formalism of the partition function. In this work, the vibrational entropy of adsorbates was explicitly calculated, Table S2.[72] The interaction of a water molecule with the active Fe and Co sites was explicitly considered. Solvent effects were evaluated for selected cases using an implicit solvent model (see Table S7 for details), which resulted in small free energy corrections of approximately 0.2 eV, Table S7. As these corrections do not significantly affect the conclusions of this study, the results presented below correspond to calculations performed without including solvent effects.

2.3. Reaction Intermediates

Within the CHE framework, valuable information about the reactivity and activity of a catalyst can be obtained from the analysis of free energy diagrams. A key approximation in this approach is the identification of the most favorable reaction mechanism. For the OER and ORR on heterogeneous catalysts and in particular on metal electrodes, it is generally assumed that the reactions typically proceed via a four-proton–electron transfer pathway involving three main intermediates: OH*, O*, and OOH*. However, alternative mechanisms are also possible, including bi-electronic processes and pathways that involve other chemical species.[73−75]

As mentioned earlier, SACs and DACs share many features with coordination compounds commonly employed in homogeneous catalysis.[76] Coordination chemistry demonstrates that a wide variety of molecular fragments can coordinate to TMs, some of which are uncommon or even impossible on extended surfaces. Recent studies have revealed that such novel reaction intermediates, also referred to as *unconventional intermediates*, can bind strongly to the active sites, forming new, stable complexes that must be considered in the analysis of the reaction profile.[20,77,78]

In the case of alkaline OER, the conventional reaction pathway is outlined in eqs. 1–4:

$$OH^- + * \rightleftharpoons OH^* + e^- \quad (1)$$

$$OH^* + OH^- \rightleftharpoons O^* + H_2O + e^- \quad (2)$$

$$O^* + OH^- \rightleftharpoons OOH^* + e^- \quad (3)$$

$$OOH^* + OH^- \rightleftharpoons O_2 + H_2O + e^- \quad (4)$$

This sequence of steps must be broadened to account for alternative mechanistic possibilities. In particular, once the OH* intermediate is formed (eq. 1), the reaction can proceed via the formation of an OH*OH* species (eq. 5), which competes with the formation of the O* intermediate (eq. 2). Similarly, an OH*O* complex may form (eq. 6), competing with the conventional OOH* intermediate (eq. 3). Furthermore, prior to the release of molecular oxygen (O_2), an oxygen complex bound to the TM (O_2*) can be generated (eqs. 7 and 8). Depending on the O–O bond distance (d_{OO}), these complexes can be classified as superoxo (η^1-O_2*, 1.25 Å

https://doi.org/10.1021/acscatal.5c08565
ACS Catal. 2026, 16, 9810−9822

< d_{00} < 1.35 Å), peroxo (η^2-O_2*, 1.35 Å < d_{00} < 1.45 Å), or dioxo (O*O*, d_{00} > 1.45 Å) species.[79,80] Finally, the oxygen complex evolves into gas-phase molecular oxygen through a chemical desorption step (eq. 9).

$$OH^* + OH^- \rightleftharpoons OH^*OH^* + e^- \quad (5)$$

$$OH^*OH^* + OH^- \rightleftharpoons OH^*O^* + H_2O + e^- \quad (6)$$

$$OOH^* + OH^- \rightleftharpoons O_2^* + H_2O + e^- \quad (7)$$

$$O^*OH^* + OH^- \rightleftharpoons O_2^* + H_2O + e^- \quad (8)$$

$$O_2^* \rightleftharpoons O_2 + * \quad (9)$$

It is common practice to assess the activity of an electrocatalyst by analyzing the reaction free energy profile. The free energy barrier of the rate-determining step (ΔG_{rds}), defined as the largest positive free energy change along a given reaction pathway, is typically used as a thermodynamic descriptor of catalytic activity. Lower ΔG_{rds} values generally indicate more promising catalysts. This approach is adopted in practically every computational study of electrocatalytic reactions. However, evaluating only the free energy barrier of the rate-determining step provides an incomplete picture and does not enable direct comparison between theory and experiment. A more rigorous approach involves using the information contained in the free energy profile to compute an observable quantity, namely the polarization curve, which allows a direct and quantitative comparison with experimental data.

2.4. Microkinetic Model and Polarization Curves

The polarization curves can be obtained using microkinetic modelling in the framework of transition state theory.[81] At each step is assigned a forward and backward kinetic constant. In the direction reported in eqs. 1−9, forward kinetic constants are linked to OER and backward kinetic constants to ORR.[82] Their expressions are, respectively:

$$k_i = \frac{K_b T}{h} e^{-\frac{\Delta G_i^{\neq}}{RT}} e^{\frac{(1-\beta)F\eta}{RT}} \quad (10)$$

$$k_{-i} = \frac{K_b T}{h} e^{-\frac{\Delta G_{-i}^{\neq}}{RT}} e^{-\frac{\beta F\eta}{RT}} \quad (11)$$

where K_b is the Boltzmann constant, T is temperature, h is the Planck constant, R is the gas constant, β is the charge transfer coefficient ($0 < \beta < 1$), F is the Faraday constant and η is the overpotential. Full details of eqs. 10 and 11 can be found in the original work.[83] $\Delta G^{\neq}$ is the activation Gibbs free energy, which is approximated to the thermodynamic barrier, i.e. the difference between adsorption Gibbs free energies between two consecutive intermediates:

$$\Delta G \approx \Delta G_{k+1} - \Delta G_k \quad (12)$$

This approximation is generally sufficient if the activation barrier is negligible compared to the thermodynamic driving force.[84−86]

The rate of each step is:

$$r_1 = k_1^+ [OH^-] N\theta_* - k_1^- N\theta_{OH^*} \quad (13)$$

$$r_2 = k_2^+ [OH^-] N\theta_{OH^*} - k_2^- N\theta_{O^*} \quad (14)$$

$$r_3 = k_3^+ [OH^-] N\theta_{O^*} - k_3^- N\theta_{OOH^*} \quad (15)$$

$$r_4 = k_4^+ [OH^-] N\theta_{OOH^*} - k_4^- N\theta_{O_2^*} \quad (16)$$

$$r_5 = k_5^+ N\theta_{O_2^*} - k_5^- [O_2] N\theta_* \quad (17)$$

where N are the moles of active site per cm^2, [OH^-] and [O_2] are the concentrations of hydroxonium and molecular oxygen respectively, and θ represents the intermediate coverages. Our model has a loading of 3% of both Fe and Co, which is sufficiently close to the value reported experimentally, about 1%.[42] For the analysis, we used the number of active sites reported experimentally, $5{\cdot}10^{13}$ per cm^2, working quantities are reported in Table S3.

The main assumption of the steady-state approximation is that the rate of formation of intermediates is equal to their rate of consumption:

$$\frac{d\theta_{OH^*}}{dt} = r_1 - r_2 = 0 \quad (18)$$

$$\frac{d\theta_{O^*}}{dt} = r_2 - r_3 = 0 \quad (19)$$

$$\frac{d\theta_{OOH^*}}{dt} = r_3 - r_4 = 0 \quad (20)$$

$$\frac{d\theta_{O_2^*}}{dt} = r_4 - r_5 = 0 \quad (21)$$

The expressions of intermediate coverages can be found by solving the system made by eqs. 18−21, considering the conservation of active sites:

$$\theta_* + \theta_{OH^*} + \theta_{O^*} + \theta_{OOH^*} + \theta_{O_2^*} = 1 \quad (22)$$

Then, the current density of OER is given by:

$$j = F(r_1 + r_2 + r_3 + r_4) \quad (23)$$

Here F is the Faraday constant. A similar treatment can be made for ORR microkinetic model, see section S4.

It must be mentioned that the symmetry of the barrier of electrochemical step can affect the overall rates calculated. Its explicitly evaluation requires to adopt potential-dependent methods such as grand canonical density functional theory approaches.[87,88] An alternative strategy is to work under the assumption of β = 0.5, which is a common approximation.[84,89,90] Furthermore, our microkinetic models consider only successive reaction steps, rather than explicitly accounting for all steps simultaneously. While this latter strategy is crucial when addressing industrially relevant chemical reactions, where multiple competing reaction pathways may be accessible under

https://doi.org/10.1021/acscatal.5c08565
ACS Catal. 2026, 16, 9810−9822

operating conditions, it is beyond the scope of the present work.[91−94] In this work, we intentionally kept the complexity of this aspect to a minimum in order to obtain easily interpretable results, while acknowledging the presence of unavoidable approximations.

3. RESULTS AND DISCUSSION

3.1. Stability of Intermediates

To deal with OER or ORR processes we have considered all possible intermediates (see eqs. 1−9) on both Fe and Co sites of the FeCo–N_3O_3@C DAC. Compared to SACs, where the active center typically coincides with the TM atom, DACs require consideration of adsorption not only on each TM site but also at positions between the two metals, the bridge sites.

After completing the screening, we found that only one additional complex with respect to the standard OH*, O*, OOH* ones, enters the game, the formation of an O_2* adduct before the release of gas-phase O_2 (last step of OER). This is also the result of interaction of O_2 with the catalyst if one looks at the process from the other direction (first step of ORR). Notably, the O_2* species exhibits an O–O bond length of 1.40 Å, with a bridge configuration between the two metal sites, Fe–O–O–Co. All other non-classical intermediates are found to be non-competitive with the standard ones (see Table 1 and Figures S2–S4). Consequently, the preferred reaction pathway for both OER and ORR involves the sequential formation of OH*, O*, OOH* and O_2* intermediates (or vice versa). Notice that oxygenated species consistently prefer to bind either on top of Co atoms or at bridge sites spanning the two metal atoms, rather than directly on top of Fe (Figure 1).

Coming to the intermediates of the OER on FeCo–N_3O_3@C, the OH* complex preferentially forms on Co with $\Delta G = -1.19$ eV, indicating the formation of a strong Co−OH chemical bond, Table 1. In contrast, the adsorption of OH* on the Fe site of the DAC is much weaker ($\Delta G = -0.25$ eV). Therefore, there is no competition between the two metal sites, OH* preferentially binds to Co.

The same is true also for OOH*, Table 1. The only exception to the preferred adsorption on Co is the O* species, which adopts a bridging configuration between Fe and Co. It is worth noting that upon adsorption of an O* species, a substantial structural rearrangement occurs around the TM atom, with one of the lattice oxygen atoms moving downward, in the direction opposite to that of the adsorbed O*, Figure 1a.

This indicates that Co is significantly more active toward O-containing species than Fe, with the latter TM playing at most an indirect role in the process. *This holds true for both the OER and ORR processes, as the thermodynamics is always governed by the most stable species.* These findings stand in sharp contrast to the results reported by Tang et al., whose model proposes that OER and ORR occur on separate sites, OER on Co and ORR on Fe.[42] Note that the much stronger Co–OH than Fe–OH bond is not an artifact of using a hybrid functional (PBE0). The large difference in adsorption free energies is also observed at the PBE level, the same functional used by Tang et al. ($\Delta G_{\text{Co-OH}} = -0.97$ eV and $\Delta G_{\text{Fe-OH}} = -0.49$ eV). Figure 1a,c show the Gibbs free energy profiles for the OER/ORR at the equilibrium potential of the reaction, $E = 1.23$ eV, relative to the Reversible Hydrogen Electrode (RHE) (see also Table 1).

Table 1. Computed Gibbs Free Energies at $E = 1.23$ V (vs RHE) and TM−O Bond Lengths of Adsorbed Intermediates on FeCo–N_3O_3@C

site	intermediate	ΔG /eV (PBE0)	d(TM−O) /Å
Fe	OH*	−0.25	1.89
	O*	0.80	1.65
	OOH*	1.36	1.82
	OH*OH*		
	O*OH*	0.77	1.84 / 1.64
	O_2*	0.47	1.85
Co	OH*	−1.19	1.80
	O*	−0.22	1.66
	OOH*	−0.09	1.78
	OH*OH*		
	O*OH*		
	O_2*	−0.19	1.76 / 1.86
bridge	OH*	−0.95	2.09 / 2.03
	O*	−0.48	1.89 / 1.73
	OOH*	0.02	2.17 / 1.98
	OH*OH*	−0.17	1.82 / 1.97
	O*OH*		
	O_2*	−0.29	1.83 / 1.87

3.2. Polarization Curves: Theory vs Experiment

In the following, we analyze this result in more detail in the attempt to reconcile the experimental evidence with theoretical modeling. Experimentally, the catalyst exhibits a high current density for the OER even at small overpotentials,[42] whereas the current density for the ORR at comparable overpotentials is substantially lower.

At first glance, the formation of the very stable OH* intermediate on Co (Figure 1a) might seem incompatible with high OER activity, since active catalysts are typically associated with labile complexes. However, the simulated polarization curves computed from DFT and microkinetic modeling (see Section) reproduce nicely the experimental ones, indicating that the catalyst is indeed highly active for the OER, Figure 1b. The apparent contradiction of a very stable intermediate with a remarkable activity of the site can be rationalized by considering that, although the formation of the OH* intermediate is highly exergonic ($\Delta G = -1.19$ eV), the subsequent thermodynamic barriers for the formation of O*, OOH*, O_2*, and ultimately O_2 are relatively moderate ($\Delta G_{\text{OH*}\rightarrow\text{O*}} = 0.70$ eV, $\Delta G_{\text{O*}\rightarrow\text{OOH*}} = 0.40$ eV, $\Delta G_{\text{OOH*}\rightarrow\text{O2*}} = -0.21$ eV and $\Delta G_{\text{O2*}\rightarrow\text{O2}} = 0.29$ eV). Thus, the strong binding of OH* does not hinder the overall reaction kinetics, as the following steps proceed with moderate energetic barriers.

In summary, the results of the DFT calculations and the microkinetic model indicate that Co is the site where the OER occurs which is precisely what has been found experimentally,[42] so no contradiction so far.

The problem arises when one considers the reverse reaction, ORR. O_2* formation, the first step of the ORR reaction, is significantly more favorable on Co than on Fe. But this is true for all intermediates and for both functionals, PBE and PBE0, except for OOH*/O*OH*, see Table S4. It is difficult to expect that the reaction occurs on another site, Fe in this case, where all involved species are less stable than whose formed on Co.

On the other hand, if one assumes that also ORR occurs on Co, it is hard to explain the moderate activity observed experimentally: the formation of a very stable Co–OH complex implies a large thermodynamic barrier to be overcome (1.19 eV) in the last step of the ORR, i.e. the evolution of OH^- from the OH* intermediate, Figure 1c. And in fact, the computed

https://doi.org/10.1021/acscatal.5c08565
ACS Catal. 2026, 16, 9810−9822

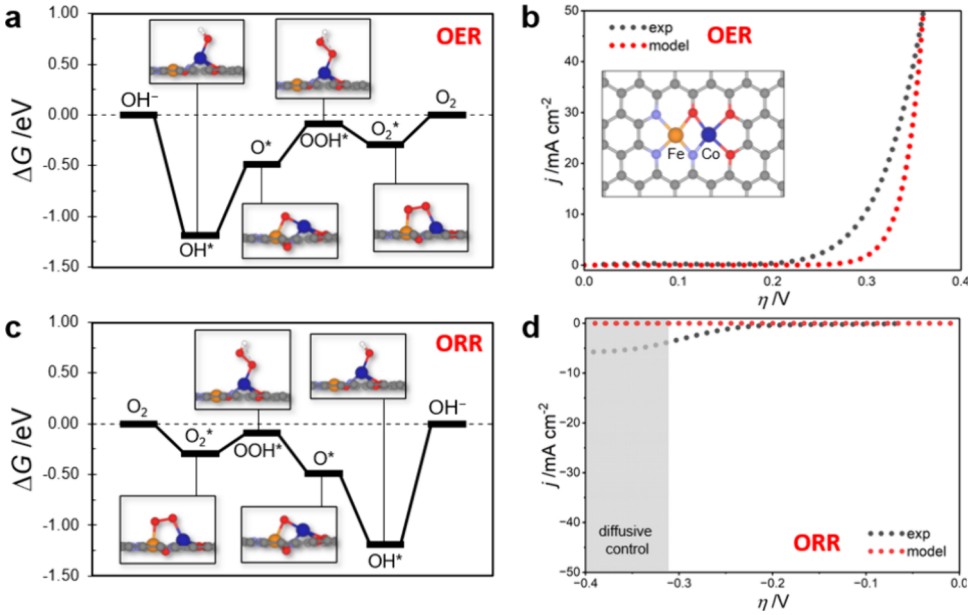

Figure 1. Active site: Co. Gibbs free energy profiles at $E = 1.23$ V (vs RHE) (a, c) and relative polarization curves (b, d) for OER and ORR on FeCo–N_3O_3@C. In grey the experimental curve, in red the simulated one. In the inset of panel (b) is reported the top-view of the FeCo–N_3O_3@C structure.

polarization curve for the ORR reaction occurring on Co shows a nearly zero current density for an overpotential between 0 and −0.4 eV, Figure 1d, at variance with the corresponding experimental curves that show a current density of −6 mA·cm^{-2} at −0.4 V. In our theoretical model of the ORR occurring on Co, the reaction starts only when the overpotential reaches −1.0 V.

Stated differently, the FeCo–N_3O_3@C DAC is active for the OER and totally inactive for the ORR, since both processes occur on the same site, the Co atom, which binds the OH species too strongly.* Fe in this model is a spectator species, it is only involved in the partial binding of the O* and O_2* intermediates in bridge positions, but it has no direct role in either the OER or the ORR processes.

3.3. New Model

Clearly, something is missing in the models used so far to describe these reactions. One often underestimated factor in this kind of problems is the role of the solvent, specifically water. Extensive literature has examined the influence of water on electrocatalytic processes. In the implicit solvent model, the solvent is treated as a continuous dielectric medium rather than as individual molecules.[95−97] In the explicit solvent model, water molecules are included explicitly, and their positions evolve dynamically according to forces computed on the fly via Ab Initio Molecular Dynamics.[98−101] Finally, in the microsolvation model, a small number of explicit solvent molecules are positioned around key regions of the active site of the catalyst, while the remainder of the solvent is neglected or treated implicitly.[102,103]

However, water does not act solely as a solvent. Indeed, single-site catalysis bridges the classical worlds of homogeneous and heterogenous catalysts.[104,105] Species of the reaction environment can therefore act as ligands, modifying the local coordination of the active phase.[106,107] This is the case of water; at the active sites of SACs and DACs containing TM atoms in positive oxidation states, water can coordinate to the TM with a strength that depends on the TM and its charge state. Motivated by this evidence, we considered if water can interact with the FeCo DAC. Indeed, we found that an H_2O molecule binds to the Fe and Co sites with adsorption free energy of about −0.30 eV. In working reaction conditions, the application of the applied potential $E = 1.23$ V (vs RHE) makes more stable the formation of an OH group bound to the Co atom. In other words, in reaction conditions it is thermodynamically favorable to have FeCo(OH*)–N_3O_3@C, where Co is bound to an OH unit ($\Delta G_{* \rightarrow OH^*} = -1.19$ eV). This means that the active phase of the catalyst changes and is no longer the same determined by various techniques before the reaction takes place.

We then evaluated the Pourbaix diagrams. It should be noted that Pourbaix diagrams are based on thermodynamic considerations and can be used to identify the most stable species at a given pH and equilibrium potential. The corresponding Pourbaix diagram is shown in Figure S5. Under the relevant reaction conditions, it is clear that the Co site is expected to be covered by OH*. This implies that, during OER, this state represents the starting point of the catalytic cycle. In contrast, under ORR conditions the Co site is effectively poisoned and cannot participate in O_2 activation; therefore, the reaction must proceed via the alternative active site associated with the Fe atom.

The presence of an OH group stably bound to Co changes completely the nature and the activity of the catalyst. We have reconsidered the formation of all possible intermediates, classical and non-classical ones, taking into account that the Co site is perturbed by the presence of the OH ligand. To a certain extent, what happens is that in operating conditions the Co site is poisoned and that this makes the Fe site, or a combination of Fe and Co sites, active for the ORR. A similar effect has been shown recently by Ye et al. who found that OH* groups can poison SACs under working conditions.[47]

https://doi.org/10.1021/acscatal.5c08565
ACS Catal. 2026, 16, 9810−9822

In studying the formation of the OER and ORR intermediates on the FeCo(OH*)–N_3O_3@C catalyst we have considered all possible sites: Fe, Co, bridge positions between Fe and Co, but also species formed on one side of the catalyst (*syn* configuration) and species formed on both sides of the two-dimensional graphene layer (*anti* configuration), see Figures S6, S7 and Tables S5, S6. *Anti*-adsorption configurations are very often more stable than *syn* configurations.

We first consider the reaction in the direction of OER on FeCo(OH*)–N_3O_3@C. The formation of the OH* intermediate, first step of OER, occurs now on the Fe site (at variance with the pristine catalyst where only Co is involved). The formation of the O* species involves both Fe and Co atoms and is slightly exergonic. Then, the reaction proceeds with formation of the OOH* species on the Fe site with a very high reaction barrier of 0.98 eV (Table 2) followed by the formation of the O_2* complex (O–O distance of 1.29 Å). From this structure, O_2 is released exergonically, $\Delta G = -0.27$ eV. Notice that this result is obtained assuming that the OH group binds to Co on one side of the catalyst, pulling the Co atom outside of the surface, while the rest of the process occurs on the other side. This implies that there is some degree of permeation of water in the structure of the catalyst, allowing the formation of *anti*-configuration adsorption modes.

From the energy profile, Figure 2a, we derived the polarization curves and compared them with the experimental results (Figure 2b). While the experiments show significant activity, the theoretical model predicts a completely inactive site (flat curve). In fact, we have previously shown that is the Co atom, in the pristine FeCo–N_3O_3@C catalyst, which is responsible for driving the OER.

If we analyze the same reaction in the ORR direction (Figure 2c,d), the process begins with the formation of O_2* and then proceeds on the available Fe site, since the Co site is now blocked by the OH ligand. The simulated polarization curves closely match the experimental data in the Faradaic region up to –0.3 V, where the experimental curve levels off due to diffusion control,[108–110] a regime that is not explicitly modelled here, Figure 2d. Polarization curves have been simulated for *syn* adsorption configurations as well, Figure S9, where it is possible to appreciate the absence of any agreement with experimental trends.

This finding is quite significant. It shows that the Fe site cannot be responsible for the ORR in the pristine catalyst — where Co forms too stable intermediates — but becomes the reactive center once, under experimental conditions, the Co site is blocked by the formation of a stable OH species.* In this sense, the FeCo–N_3O_3@C catalyst operates in a truly concerted manner: Co drives the OER, while Fe takes over the ORR, as a direct consequence of the structural changes induced by the reaction with water. It is essential to emphasize that the direct interpretation of the dual nature of the active site under oxygen evolution and oxygen reduction reactions is possible only through explicit simulation of polarization curves, as the solely thermodynamic analysis is insufficient. The calculated OER polarization curve following the pathway reported in Figure 2a is not compatible with the values measured experimentally, at variance to what happens considering OER on the Co-site, Figure 1a. This rationalization of the mechanism through the simulated polarization curves can explain the OER pathway on the Co site.

There is another aspect that deserves some comment: the experimental OER current is higher than the ORR current.[42] For example, at an applied overpotential of 0.3 V, the OER current reaches 11 mA cm^{-2}, whereas the corresponding ORR current is −3 mA cm^{-2}. However, if one looks at the reaction profiles, Figure 1a (OER on Co) and 2c (ORR on Fe), this difference is hard to explain. In fact, in the case of the OER, which takes place on the Co atom, the highest barrier is 0.70 eV, only slightly larger than that of the ORR occurring on the Fe site (0.52 eV). This is an example of the importance of microkinetic modeling. The higher OER currents arise from the combined effect of multiple energy barriers along the reaction pathway, a concept that has also been highlighted in previous studies.[82,111] Once again, focusing solely on the highest barrier is not enough to draw reliable conclusions about the overall catalytic activity.

Table 2. Computed Gibbs Free Energies at $E = 1.23$ V (vs RHE) and TM-O Bond Length of Adsorbed Intermediates with *anti*-Configuration (When Two Adsorbates are Present) on FeCo(OH*)–N_3O_3@C

site	intermediate	ΔG /eV (PBE0)	d(TM−O) /Å
Fe	OH*	−0.11	1.85
bridge	O*	−0.20	1.64
Fe	OOH*	0.78	1.84
Co / Fe	OH*OH*	0.42	1.80 / 1.92
Co / Fe	O*OH*	1.01	1.81 / 1.87
Fe	O_2*	0.27	1.82

3.4. Comparison with Experimental XANES Spectra

The DFT results, combined with the microkinetic model, reveal a revised mechanism for the OER and ORR on the FeCo–N_3O_3@C DAC. Co acts as the active site during the OER and Fe during the ORR, but only as a result of structural rearrangements of the catalyst under reaction conditions. The main difference from the original interpretation proposed by Tang et al.[42] lies in the fact that the pristine FeCo–N_3O_3@C cannot simultaneously account for OER and ORR activity on two distinct sites, as Co exhibits a much higher affinity than Fe for binding oxygenated species. The strongest evidence for a synergistic role of Fe and Co in both processes arises from the analysis of XANES data,[42] and the revised model proposed here is consistent with these observations.

Experimentally, relative to the pristine state, the Co K-edge XANES spectra during the OER and the Fe K-edge spectra during the ORR exhibit small positive energy shifts, on the order of a few tenths of an eV. In contrast, the Co K-edge spectra during the ORR and the Fe K-edge spectra during the OER show negligible changes compared to the pristine catalyst.[42] These shifts are attributed to the formation of oxygenated intermediates, as O-containing species increase the positive charge on Fe or Co, leading to corresponding positive shifts in their XANES edges. XANES inherently measures the weighted average of all species containing the absorbing atom (Co or Fe), with the relative fractions of each species serving as weights. Consequently, the recorded spectra represent linear combinations of all intermediates, dominated by the most abundant species.

To evaluate the contribution of the different species, we analysed the catalyst surface coverages of the intermediates involved in the OER and ORR across the range of applied potentials, as obtained from the microkinetic model

https://doi.org/10.1021/acscatal.5c08565
ACS Catal. 2026, 16, 9810−9822

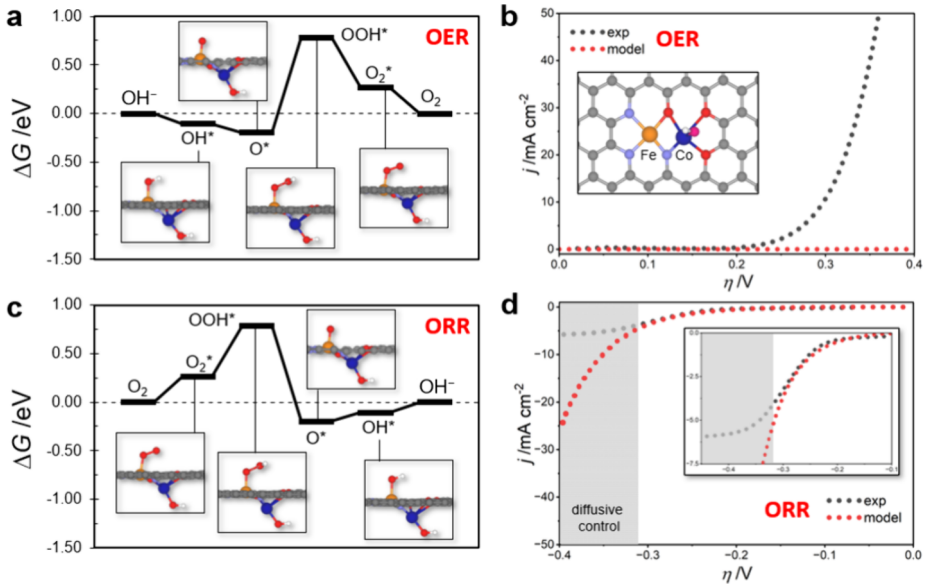

Figure 2. Active site: Fe. Gibbs free energy profiles at $E = 1.23$ V (vs RHE) (a, c) and relative polarization curves (b, d) for OER and ORR on FeCo(OH*)–N_3O_3@C. In grey the experimental curve, in red the simulated one. In the inset of panel b is reported the top-view of the FeCo(OH*)–N_3O_3@C structure.

(Figure 3). This approach enables a direct correlation between the observed XANES shifts and the variations in the atomic charges of Fe and Co associated with the formation of the most abundant, long-lived oxygenated intermediates. The atomic charges were computed using the Quantum Theory of Atoms in Molecules (QTAIM).[112−115] For the OER, where Co serves as the active site, the dominant surface species is the OH* intermediate (Figure 4a). This can be intuitively rationalized by the fact that OH* corresponds to a deep minimum on the potential energy profile, requiring relatively high barriers to proceed to subsequent reaction steps (Figure 1a). Such conditions typically favor the formation of long-lived intermediates. The associated change in the Bader charge of Co (+0.27 *e*) is considerably larger than that of Fe (+0.11 *e*), relative to the as-prepared FeCo–N_3O_3@C catalyst, consistent with the observed shift in the Co K-edge XANES spectra.

In contrast, for the ORR, where Fe acts as the active site, two intermediates, OH* and O*, exhibit longer lifetimes and thus higher surface coverages (Figure 4b). These species correspond to deeper minima on the potential energy surface (Figure 2b). In both cases, the change in Bader charge on Fe (+0.20 *e* and +0.22 *e*, respectively) significantly exceeds that on Co (−0.02 *e* and +0.04 *e*, respectively), with values referenced to the FeCo(OH*)–N_3O_3@C catalyst formed under operando conditions. This behavior agrees with the observed shift in the Fe K-edge XANES spectra. Although additional factors may contribute to the XANES shifts, the present analysis demonstrates that the proposed model aligns well with the experimental spectra reported by Tang et al. [42]

3.5. Fe−Co Synergy

Before concluding, we examined the potential synergistic effects between Fe and Co atoms in the dual-atom catalyst (DAC), in comparison with their isolated counterparts, Fe and Co single-atom catalysts (SACs). To this end, we designed a computational experiment in which the two key reactions, OER on Co and ORR on Fe, were re-evaluated as if they occurred on catalysts containing only the respective single active metal sites. Specifically, for Co we modeled an O-doped graphene layer where Co adopts a square-planar coordination with four O atoms (Co–O_4@C), closely resembling the local coordination environment in the FeCo–N_3O_3@C DAC, Figures S10, S11, and Table S8. For Fe, we constructed an N-doped graphene matrix with Fe in a square-planar Fe–N_4 configuration (Fe–N_4@C), Figures S12, S13, and Table S9. The corresponding reaction energy profiles were then compared with those obtained for the FeCo–N_3O_3@C DAC (Figure 4).

It is immediately apparent that the OER on the Co site of the DAC proceeds with significantly lower thermodynamic barriers than on the analogous Co–O_4@C SAC. In particular, the highest energy barrier decreases from 1.24 eV in the Co–O_4@C SAC to 0.70 eV in the DAC (Figure 4a). A similar trend is observed for the ORR on Fe: the largest barrier on Fe–N_4@C (1.28 eV) is roughly 2.5 times higher than that on the DAC (Figure 4b).

These findings clearly demonstrate that the proximity of the two neighboring transition-metal atoms not only enables a *Janus-type* dual reaction pathway but also induces a mutual electronic interaction that enhances the overall catalytic reactivity of the system.

4. CONCLUSIONS

In this study, we investigated the significance of accounting for the potential changes of single-site catalysts under working conditions. As a model system, we examined the dual-atom catalyst FeCo–N_3O_3@C, whose as-prepared structure was characterized with atomistic precision and whose reactivity was evaluated in both the oxygen evolution (OER) and oxygen reduction (ORR) reactions. To this end, we performed quantum chemical calculations at the DFT level, complemented by microkinetic modeling, to derive theoretical polarization curves.

https://doi.org/10.1021/acscatal.5c08565
ACS Catal. 2026, 16, 9810−9822

Our results yield several key insights. First, all oxygenate species, both classical and non-classical, formed during the OER and ORR bind significantly more strongly to the Co site than to the Fe site in FeCo–N_3O_3@C. Consequently, the enhanced stability of these intermediates drives both the forward (OER) and reverse (ORR) reactions to occur predominantly on Co, while Fe largely acts as a spectator. Although the computed polarization curves reproduce the experimental OER behavior well, they fail to predict any ORR activity, in contrast to experiment. This discrepancy is unsurprising, as a catalyst optimized for one reaction direction typically performs poorly in the reverse process, and the Co site in FeCo–N_3O_3@C is no exception.

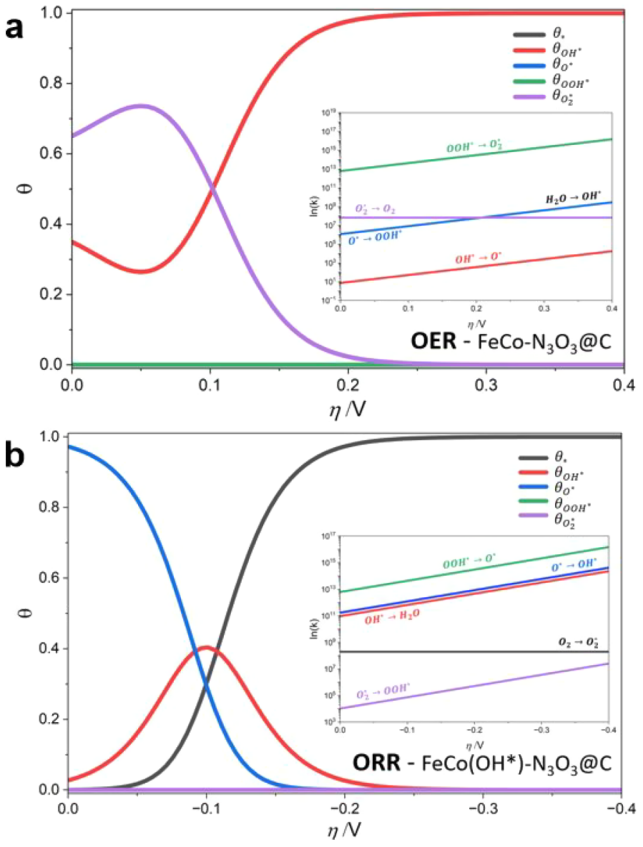

Figure 3. (a) Calculated surface coverage of adsorbed intermediates during OER on FeCo–N_3O_3@C. The surface is predominantly covered by OH*, indicating that this intermediate plays a key role in the reaction pathway. This observation aligns with the trend of the kinetic constant for the OH* → O* transformation shown in the inset. (b) Calculated surface coverage of adsorbed intermediates during ORR on FeCo(OH*)–N_3O_3@C. The surface is mainly covered by O* and OH* species. At lower overpotentials, the Fe site remains largely unoccupied, consistent with OOH* formation being the rate-determining step, as illustrated in the inset.

However, under applied potentials relevant to the reaction, water, though weakly adsorbed on both Fe and Co, spontaneously dissociates to form OH*, resulting in a highly stable Co–OH adduct. This species effectively blocks the Co site for the ORR, since water desorption is associated with a prohibitively high barrier. As a result, the ORR shifts to the Fe site, where it proceeds with low thermodynamic barriers. The corresponding computed polarization curves are now in excellent agreement with experimental observations.

To validate our theoretical findings, we rationalized the shifts observed in the Co and Fe K-edge XANES spectra by analyzing the variations in Bader charges of the dominant intermediate species and their respective surface coverages. This approach enables the disentanglement of the various contributions to the XANES features.

By comparing the predicted activity of FeCo–N_3O_3@C in OER and ORR with that of hypothetical Co–O_4@C and Fe–N_4@C single-atom catalysts, we further demonstrated that the exceptional performance of the dual-atom catalyst arises from the synergistic interaction between the neighboring Fe and Co atoms. This synergy is also evident from several intermediates that adopt bridging configurations between the two metal centers.

Importantly, this mechanistic insight could not have been obtained without explicitly simulating polarization curves. A purely static analysis based on reaction profiles, as is commonly performed, would have led to incorrect conclusions regarding the true catalytically active sites.

Overall, our findings emphasize the importance of accounting for the structural and chemical changes that a catalyst undergoes under reaction conditions to accurately elucidate catalytic mechanisms. The active phase can differ significantly from the as-prepared material, as in this case, where water dissociation leads to the formation of stable Co–OH complexes. Thus, the true active phase corresponds to pristine FeCo–N_3O_3@C during OER, but to its modified form, FeCo(OH*)–N_3O_3@C, during ORR.

In is important to underline that the study works under the assumption that the system can be reliably described by

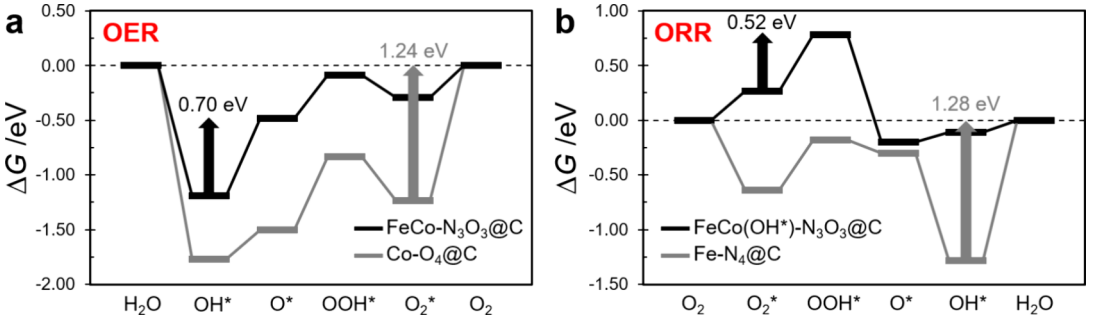

Figure 4. (a) Calculated Gibbs free energy profiles at $E = 1.23$ V (vs RHE) for the OER on FeCo–N_3O_3@C (black line, reaction occurring on Co) and Co–O_4@C (grey line). (b) Calculated Gibbs free energy profiles at $E = 1.23$ V (vs RHE) for the ORR on FeCo(OH*)–N_3O_3@C (black line, reaction occurring on Fe) and Fe–N_4@C (grey line). Computed Gibbs free energies are reported in Tables 1,2 and S8,S9 of SI.

https://doi.org/10.1021/acscatal.5c08565
ACS Catal. 2026, 16, 9810−9822

graphene nanosheets, that are nowadays widespread in catalysis research.[116−118] Future work will be devoted to the investigation of more subtle effects such as the role of supporting electrolyte, the presence of interlayers and the possible penetration of reactive species and solvent molecules.

This work provides a clear demonstration of the dynamic behaviour of catalysts comprising isolated transition-metal atoms embedded in carbon matrices. The implications extend broadly to other catalytic systems and electrochemical reactions, underscoring the importance of accounting for possible structural changes of the active site in the course of the reaction.

■ ASSOCIATED CONTENT

Data Availability Statement

The data supporting this study can be obtained from the ESI and can be asked to the authors upon reasonable request. The home-made code used to perform microkinetic modelling can be obtained by asking to the authors.

Supporting Information

The Supporting Information is available free of charge at https://pubs.acs.org/doi/10.1021/acscatal.5c08565.

Supplementary tables, figures and Cartesian coordinates; computational details; more details on simulated species; microkinetic modelling; and Cartesian coordinates of the catalysts (PDF)

■ AUTHOR INFORMATION

Corresponding Authors

Gianfranco Pacchioni − *Department of Materials Science, University of Milan-Bicocca, via R. Cozzi 55, Milano 20125, Italy*; orcid.org/0000-0002-4749-0751; Email: gianfranco.pacchioni@unimib.it

Giovanni Di Liberto − *Department of Materials Science, University of Milan-Bicocca, via R. Cozzi 55, Milano 20125, Italy*; orcid.org/0000-0003-4289-2732; Email: giovanni.diliberto@unimib.it

Authors

Elisabetta Inico − *Department of Materials Science, University of Milan-Bicocca, via R. Cozzi 55, Milano 20125, Italy*

Matteo Spotti − *Department of Materials Science, University of Milan-Bicocca, via R. Cozzi 55, Milano 20125, Italy*

Complete contact information is available at: https://pubs.acs.org/doi/10.1021/acscatal.5c08565

Author Contributions

†EI and MS equally contributed to this work. The manuscript was written through contributions of all authors.

Notes

The authors declare no competing financial interest.

■ ACKNOWLEDGMENTS

We thank Prof. Elisa Borfecchia for useful discussions on XANES spectra. GDL has received funding through the PRIN project "SACtoH2" (project code P2022AZETB by the Italian Ministry for Universities and Research (MUR), in the context of the National Recovery and Resilience Plan and co-financed by the European Commission - Next Generation EU (Mission 4, Component 1). Access to the CINECA supercomputing resources was granted *via* ISCRAB and EuroHPC regular access projects.

■ REFERENCES

(1) Boyes, E. D.; LaGrow, A. P.; Ward, M. R.; Mitchell, R. W.; Gai, P. L. Single Atom Dynamics in Chemical Reactions. *Acc. Chem. Res.* **2020**, *53* (2), 390–399.

(2) Chen, L.; Allec, S. I.; Nguyen, M.-T.; Kovarik, L.; Hoffman, A. S.; Hong, J.; Meira, D.; Shi, H.; Bare, S. R.; Glezakou, V.-A.; Rousseau, R.; Szanyi, J. Dynamic Evolution of Palladium Single Atoms on Anatase Titania Support Determines the Reverse Water–Gas Shift Activity. *J. Am. Chem. Soc.* **2023**, *145* (19), 10847–10860.

(3) Zhou, T.; Yan, H.; Li, W.; Zhang, W.; He, H.; Hu, S.; Wang, R.; Xiao, T.; Liu, L.; Zhang, L.; Wu, W.; Liu, C.; Zheng, X.; Pan, Y.; Zeng, J.; Li, X. Reaction-Induced Dynamic Evolution of PtIn/SiO_2 Catalyst for Propane Dehydrogenation. *Nat. Commun.* **2025**, *16* (1), 5153.

(4) Viñes, F.; Gomes, J. R. B.; Illas, F. Understanding the Reactivity of Metallic Nanoparticles: Beyond the Extended Surface Model for Catalysis. *Chem. Soc. Rev.* **2014**, 4922–4939.

(5) Wang, A.; Li, J.; Zhang, T. Heterogeneous Single-Atom Catalysis. *Nat. Rev. Chem.* **2018**, *2* (6), 65–81.

(6) Kraushofer, F.; Parkinson, G. S. Single-Atom Catalysis: Insights from Model Systems. *Chem. Rev.* **2022**, *122* (18), 14911–14939.

(7) Kaiser, S. K.; Chen, Z.; Faust Akl, D.; Mitchell, S.; Pérez-Ramírez, J. Single-Atom Catalysts across the Periodic Table. *Chem. Rev.* **2020**, *120* (21), 11703–11809.

(8) Singh, B.; Gawande, M. B.; Kute, A. D.; Varma, R. S.; Fornasiero, P.; McNeice, P.; Jagadeesh, R. V.; Beller, M.; Zbořil, R. Single-Atom (Iron-Based) Catalysts: Synthesis and Applications. *Chem. Rev.* **2021**, *121* (21), 13620–13697.

(9) Qiao, B.; Wang, A.; Yang, X.; Allard, L. F.; Jiang, Z.; Cui, Y.; Liu, J.; Li, J.; Zhang, T. Single-Atom Catalysis of CO Oxidation Using Pt1/FeOx. *Nat. Chem.* **2011**, *3* (8), 634–641.

(10) Copéret, C.; Chabanas, M.; Petroff Saint-Arroman, R.; Basset, J.-M. Homogeneous and Heterogeneous Catalysis: Bridging the Gap through Surface Organometallic Chemistry. *Angew. Chem., Int. Ed.* **2003**, *42* (2), 156–181.

(11) Cui, X.; Li, W.; Ryabchuk, P.; Junge, K.; Beller, M. Bridging Homogeneous and Heterogeneous Catalysis by Heterogeneous Single-Metal-Site Catalysts. *Nat. Catal.* **2018**, *1* (6), 385–397.

(12) Iemhoff, A.; Vennewald, M.; Palkovits, R. Single-Atom Catalysts on Covalent Triazine Frameworks: At the Crossroad between Homogeneous and Heterogeneous Catalysis. *Angew. Chem., Int. Ed.* **2023**, *62* (7), No. e202212015.

(13) Timoshenko, J.; Roldan Cuenya, B. *In Situ* / *Operando* Electrocatalyst Characterization by X-Ray Absorption Spectroscopy. *Chem. Rev.* **2021**, *121* (2), 882–961.

(14) Chee, S. W.; Lunkenbein, T.; Schlögl, R.; Roldán Cuenya, B. *Operando* Electron Microscopy of Catalysts: The Missing Cornerstone in Heterogeneous Catalysis Research? *Chem. Rev.* **2023**, *123* (23), 13374–13418.

(15) Actis, A.; Melchionna, M.; Filippini, G.; Fornasiero, P.; Prato, M.; Salvadori, E.; Chiesa, M. Morphology and Light-Dependent Spatial Distribution of Spin Defects in Carbon Nitride. *Angew. Chem., Int. Ed.* **2022**, *61* (43), No. e202210640.

(16) DeRita, L.; Resasco, J.; Dai, S.; Boubnov, A.; Thang, H. V.; Hoffman, A. S.; Ro, I.; Graham, G. W.; Bare, S. R.; Pacchioni, G.; Pan, X.; Christopher, P. Structural Evolution of Atomically Dispersed Pt Catalysts Dictates Reactivity. *Nat. Mater.* **2019**, *18* (7), 746–751.

(17) Koppe, J.; Yakimov, A. V.; Gioffrè, D.; Usteri, M.-E.; Vosegaard, T.; Pintacuda, G.; Lesage, A.; Pell, A. J.; Mitchell, S.; Pérez-Ramírez, J.; Copéret, C. Coordination Environments of Pt Single-Atom Catalysts from NMR Signatures. *Nature* **2025**, *642* (8068), 613–619.

(18) Li, L.; Chang, X.; Lin, X.; Zhao, Z.-J.; Gong, J. Theoretical Insights into Single-Atom Catalysts. *Chem. Soc. Rev.* **2020**, *49* (22), 8156–8178.

(19) Zhuo, H.-Y.; Zhang, X.; Liang, J.-X.; Yu, Q.; Xiao, H.; Li, J. Theoretical Understandings of Graphene-Based Metal Single-Atom Catalysts: Stability and Catalytic Performance. *Chem. Rev.* **2020**, *120* (21), 12315–12341.
(20) Di Liberto, G.; Pacchioni, G. Modeling Single-Atom Catalysis. *Adv. Mater.* **2023**, *35* (46), No. 2307150.
(21) Allasia, N.; Xu, S.; Jafri, S. F.; Borfecchia, E.; Cipriano, L. A.; Terraneo, G.; Tosoni, S.; Mino, L.; Di Liberto, G.; Pacchioni, G.; Vilé, G. Resolving the Nanostructure of Carbon Nitride-Supported Single-Atom Catalysts. *Small* **2025**, *21* (23).
(22) He, T.; Santiago, A. R. P.; Kong, Y.; Ahsan, M. A.; Luque, R.; Du, A.; Pan, H. Atomically Dispersed Heteronuclear Dual-Atom Catalysts: A New Rising Star in Atomic Catalysis. *Small* **2022**, *18* (12).
(23) Wang, J.; Zhao, C.-X.; Liu, J.-N.; Song, Y.-W.; Huang, J.-Q.; Li, B.-Q. Dual-Atom Catalysts for Oxygen Electrocatalysis. *Nano Energy* **2022**, *104*, No. 107927.
(24) Li, L.; Yuan, K.; Chen, Y. Breaking the Scaling Relationship Limit: From Single-Atom to Dual-Atom Catalysts. *Acc. Mater. Res.* **2022**, *3* (6), 584–596.
(25) Chen, Z.; Liao, X.; Sun, C.; Zhao, K.; Ye, D.; Li, J.; Wu, G.; Fang, J.; Zhao, H.; Zhang, J. Enhanced Performance of Atomically Dispersed Dual-Site Fe-Mn Electrocatalysts through Cascade Reaction Mechanism. *Appl. Catal. B* **2021**, *288*, No. 120021.
(26) Li, R.; Wang, D. Superiority of Dual-Atom Catalysts in Electrocatalysis: One Step Further Than Single-Atom Catalysts. *Adv. Energy Mater.* **2022**, *12* (9), No. 2103564.
(27) Fu, J.; Dong, J.; Si, R.; Sun, K.; Zhang, J.; Li, M.; Yu, N.; Zhang, B.; Humphrey, M. G.; Fu, Q.; Huang, J. Synergistic Effects for Enhanced Catalysis in a Dual Single-Atom Catalyst. *ACS Catal.* **2021**, *11* (4), 1952–1961.
(28) Giulimondi, V.; Ruiz-Ferrando, A.; Clark, A. H.; Kaiser, S. K.; Krumeich, F.; Martín, A. J.; López, N.; Pérez-Ramírez, J. Catalytic Synergies in Bimetallic Ru-Pt Single–Atom Catalysts via Speciation Control. *Adv. Funct. Mater.* **2022**, *32* (52), No. 2206513.
(29) Di Liberto, G.; Cipriano, L. A.; Pacchioni, G. Single Atom Catalysts: What Matters Most, the Active Site or The Surrounding?. *ChemCatChem* **2022**, *14* (19), No. e202200611.
(30) Lätsch, L.; Guda, S. A.; Romankov, V.; Wartmann, C.; Neudörfl, J. M.; Dreiser, J.; Berkessel, A.; Guda, A. A.; Copéret, C. Tracking Coordination Environment and Reaction Intermediates in Homogeneous and Heterogeneous Epoxidation Catalysts via Ti L2,3-Edge Near-Edge X-Ray Absorption Fine Structures. *J. Am. Chem. Soc.* **2024**, *146* (11), 7456–7466.
(31) Abbet, S.; Sanchez, A.; Heiz, U.; Schneider, W. D.; Ferrari, A. M.; Pacchioni, G.; Rösch, N. Acetylene Cyclotrimerization on Supported Size-Selected Pd(n) Clusters ($1 \leq n \leq 30$): One Atom Is Enough!. *J. Am. Chem. Soc.* **2000**, *122* (14), 3453–3457.
(32) Calle-Vallejo, F.; Koper, M. T. M.; Bandarenka, A. S. Tailoring the Catalytic Activity of Electrodes with Monolayer Amounts of Foreign Metals. *Chem. Soc. Rev.* **2013**, *42* (12), 5210–5230.
(33) Shao, Y.; Yuan, Q.; Zhou, J. Single-Atom Catalysts and Dual-Atom Catalysts for CO_2 Electroreduction: Competition or Cooperation? *Small* **2023**, *19* (40), No. 2303446.
(34) Gu, T.; Zhang, D.; Yang, Y.; Peng, C.; Xue, D.; Zhi, C.; Zhu, M.; Liu, J. Dual-Sites Coordination Engineering of Single Atom Catalysts for Full-Temperature Adaptive Flexible Ultralong-Life Solid-State Zn−Air Batteries. *Adv. Funct. Mater.* **2023**, *33* (8), No. 2212299.
(35) Tosello Gardini, A.; Raucci, U.; Parrinello, M. Machine Learning-Driven Molecular Dynamics Unveils a Bulk Phase Transformation Driving Ammonia Synthesis on Barium Hydride. *Nat. Commun.* **2025**, *16* (1), 2475.
(36) Yang, M.; Raucci, U.; Parrinello, M. Reactant-Induced Dynamics of Lithium Imide Surfaces during the Ammonia Decomposition Process. *Nat. Catal.* **2023**, *6* (9), 829–836.
(37) Han, Y.; Wei, Y.; Goswami, A.; Alexandrova, A. Uncovering the True Active Sites in Ni–N–C Catalysts for CO_2 Electroreduction. *J. Am. Chem. Soc.* **2025**, *147* (42), 38636–38646.
(38) Zhang, W.; Yi, S.; Yu, Y.; Liu, H.; Kucernak, A.; Wu, J.; Li, S. Fe-Based Dual-Atom Catalysts for the Oxygen Reduction Reaction. *J. Mater. Chem. A Mater.* **2024**, *12* (1), 87–112.
(39) He, Y.; Yang, X.; Li, Y.; Liu, L.; Guo, S.; Shu, C.; Liu, F.; Liu, Y.; Tan, Q.; Wu, G. Atomically Dispersed Fe–Co Dual Metal Sites as Bifunctional Oxygen Electrocatalysts for Rechargeable and Flexible Zn–Air Batteries. *ACS Catal.* **2022**, *12* (2), 1216–1227.
(40) Zhang, L.; Dong, Y.; Li, L.; Wei, L.; Su, J.; Guo, L. Enhanced Oxygen Reduction Activity and Stability of Double-Layer Nitrogen-Doped Carbon Catalyst with Abundant Fe-Co Dual-Atom Sites. *Nano Energy* **2023**, *117*, No. 108854.
(41) Yuan, L.-J.; Miao, Z.-Y.; Sui, X.-L.; Lee, C.-F.; Li, Q.; Yin, M.-J.; Shen, L.-X.; Lu, Y.-R.; Zhao, Z.-G.; Liu, Y.-Z.; Zhu, L.-S.; Gong, W.; Feng, W.-L.; Wang, H.-T.; Zhang, G.-X.; Wang, Z.-B. Janus Effect of FeCo Dual Atom Catalyst with Co as Active Center in Acidic Oxygen Reduction Reaction. *Nat. Commun.* **2025**, *16* (1), 7198.
(42) Tang, B.; Zhou, Y.; Ji, Q.; Zhuang, Z.; Zhang, L.; Wang, C.; Hu, H.; Wang, H.; Mei, B.; Song, F.; Yang, S.; Weckhuysen, B. M.; Tan, H.; Wang, D.; Yan, W. A Janus Dual-Atom Catalyst for Electrocatalytic Oxygen Reduction and Evolution. *Nat. Synth.* **2024**, *3* (7), 878–890.
(43) Saetta, C.; Barlocco, I.; Liberto, G.; Di; Pacchioni, G. Key Ingredients for the Screening of Single Atom Catalysts for the Hydrogen Evolution Reaction: The Case of Titanium Nitride. *Small* **2024**, *20*, No. 2401058.
(44) Barlocco, I.; Di Liberto, G.; Pacchioni, G. New Scaling Relationships for the Oxygen Evolution Reaction on Single Atom Catalysts. *Catal. Today* **2024**, *427*, No. 114409.
(45) Misra, D.; Di Liberto, G.; Pacchioni, G. CO_2 Electroreduction on Single Atom Catalysts: Is Water Just a Solvent?. *J. Catal.* **2023**, *422*, 1–11.
(46) Bonardi, A.; Xu, S.; Di Liberto, G.; Pacchioni, G. Role of Water in Modulating the Fe^{3+}/Fe^{2+} Redox Couple in Iron-Based Complexes and Single-Atom Catalysts. *J. Phys. Chem. Lett.* **2025**, *16* (39), 10049–10057.
(47) Ye, S.; Liu, F.; She, F.; Chen, J.; Zhang, D.; Kumatani, A.; Shiku, H.; Wei, L.; Li, H. Hydrogen Binding Energy Is Insufficient for Describing Hydrogen Evolution on Single-Atom Catalysts. *Angew. Chem., Int. Ed.* **2025**, *64* (23), No. e202425402.
(48) Kresse, G.; Hafner, J. *Ab Initio* Molecular Dynamics for Liquid Metals. *Phys. Rev. B* **1993**, *47* (1), 558–561.
(49) Kresse, G.; Hafner, J. *Ab Initio* Molecular-Dynamics Simulation of the Liquid-Metal–Amorphous-Semiconductor Transition in Germanium. *Phys. Rev. B* **1994**, *49* (20), 14251–14269.
(50) Kresse, G.; Furthmüller, J. Efficiency of Ab-Initio Total Energy Calculations for Metals and Semiconductors Using a Plane-Wave Basis Set. *Comput. Mater. Sci.* **1996**, *6* (1), 15–50.
(51) Perdew, J. P.; Burke, K.; Ernzerhof, M. Generalized Gradient Approximation Made Simple. *Phys. Rev. Lett.* **1996**, *77* (18), 3865–3868.
(52) Blöchl, P. E. Projector Augmented-Wave Method. *Phys. Rev. B* **1994**, *50* (24), 17953–17979.
(53) Kresse, G.; Joubert, D. From Ultrasoft Pseudopotentials to the Projector Augmented-Wave Method. *Phys. Rev. B* **1999**, *59* (3), 1758–1775.
(54) Monkhorst, H. J.; Pack, J. D. *Special Points for Brillonin-Zone Integrations**, **1976**; Vol. 13.
(55) Grimme, S.; Antony, J.; Ehrlich, S.; Krieg, H. A Consistent and Accurate Ab Initio Parametrization of Density Functional Dispersion Correction (DFT-D) for the 94 Elements H-Pu. *J. Chem. Phys.* **2010**, *132* (15), No. 154104.
(56) Adamo, C.; Barone, V. Toward Reliable Density Functional Methods without Adjustable Parameters: The PBE0 Model. *J. Chem. Phys.* **1999**, *110* (13), 6158–6170.
(57) Perdew, J. P.; Ernzerhof, M.; Burke, K. Rationale for Mixing Exact Exchange with Density Functional Approximations. *J. Chem. Phys.* **1996**, *105* (22), 9982–9985.

https://doi.org/10.1021/acscatal.5c08565
ACS Catal. 2026, 16, 9810−9822

(58) Di Liberto, G.; Cipriano, L. A.; Pacchioni, G. Universal Principles for the Rational Design of Single Atom Electrocatalysts? Handle with Care. *ACS Catal.* **2022**, 5846–5856.
(59) Barlocco, I.; Cipriano, L. A.; Di Liberto, G.; Pacchioni, G. Modeling Hydrogen and Oxygen Evolution Reactions on Single Atom Catalysts with Density Functional Theory: Role of the Functional. *Adv. Theory Simul.* **2022**, *6*, No. 2200513.
(60) Patel, A. M.; Ringe, S.; Siahrostami, S.; Bajdich, M.; Nørskov, J. K.; Kulkarni, A. R. Theoretical Approaches to Describing the Oxygen Reduction Reaction Activity of Single-Atom Catalysts. *J. Phys. Chem. C* **2018**, *122* (51), 29307–29318.
(61) Basset, J.-M.; Lefebvre, F.; Santini, C. Surface Organometallic Chemistry: Some Fundamental Features Including the Coordination Effects of the Support. *Coord. Chem. Rev.* **1998**, *178–180*, 1703–1723.
(62) Zhang, Y.; Yang, J.; Ge, R.; Zhang, J.; Cairney, J. M.; Li, Y.; Zhu, M.; Li, S.; Li, W. The Effect of Coordination Environment on the Activity and Selectivity of Single-Atom Catalysts. *Coord. Chem. Rev.* **2022**, *461*, No. 214493.
(63) Zhang, J.; Yang, H.; Liu, B. Coordination Engineering of Single-Atom Catalysts for the Oxygen Reduction Reaction: A Review. *Adv. Energy Mater.* **2021**, *11* (3), No. 2002473.
(64) Nørskov, J. K.; Rossmeisl, J.; Logadottir, A.; Lindqvist, L.; Kitchin, J. R.; Bligaard, T.; Jónsson, H. Origin of the Overpotential for Oxygen Reduction at a Fuel-Cell Cathode. *J. Phys. Chem. B* **2004**, *108* (46), 17886–17892.
(65) Nørskov, J. K.; Bligaard, T.; Logadottir, A.; Bahn, S.; Hansen, L. B.; Bollinger, M.; Bengaard, H.; Hammer, B.; Sljivancanin, Z.; Mavrikakis, M.; Xu, Y.; Dahl, S.; Jacobsen, C. J. H. Universality in Heterogeneous Catalysis. *J. Catal.* **2002**, *209* (2), 275–278.
(66) Norskov, J. K.; Christensen, C. H. Toward Efficient Hydrogen Production at Surfaces. *Science (1979).*, **2006**, *312* (5778), 1322–1323.
(67) Rossmeisl, J.; Logadottir, A.; Nørskov, J. K. Electrolysis of Water on (Oxidized) Metal Surfaces. *Chem. Phys.* **2005**, *319* (1–3), 178–184.
(68) Kulkarni, A.; Siahrostami, S.; Patel, A.; Nørskov, J. K. Understanding Catalytic Activity Trends in the Oxygen Reduction Reaction. *Chem. Rev.* **2018**, 2302–2312.
(69) Liu, X.; Xiao, J.; Peng, H.; Hong, X.; Chan, K.; Nørskov, J. K. Understanding Trends in Electrochemical Carbon Dioxide Reduction Rates. *Nat. Commun.* **2017**, *8*, 15438.
(70) Peterson, A. A.; Abild-Pedersen, F.; Studt, F.; Rossmeisl, J.; Nørskov, J. K. How Copper Catalyzes the Electroreduction of Carbon Dioxide into Hydrocarbon Fuels. *Energy Environ. Sci.* **2010**, *3* (9), 1311–1315.
(71) Studt, F.; Abild-Pedersen, F.; Bligaard, T.; Sørensen, R. Z.; Christensen, C. H.; Nørskov, J. K. Identification of Non-Precious Metal Alloy Catalysts for Selective Hydrogenation of Acetylene. *Science (1979).* **2008**, *320* (5881), 1320–1322.
(72) Di Simone, E.; Vilé, G.; Di Liberto, G.; Pacchioni, G. Decoding the Role of Adsorbates Entropy in the Reactivity of Single-Atom Catalysts. *ACS Catal.* **2025**, *15* (1), 447–456.
(73) Barlocco, I.; Cipriano, L. A.; Di Liberto, G.; Pacchioni, G. Does the Oxygen Evolution Reaction Follow the Classical OH*, O*, OOH* Path on Single Atom Catalysts?. *J. Catal.* **2023**, *417*, 351–359.
(74) Cipriano, L. A.; Di Liberto, G.; Pacchioni, G. Superoxo and Peroxo Complexes on Single-Atom Catalysts: Impact on the Oxygen Evolution Reaction. *ACS Catal.* **2022**, *12* (19), 11682–11691.
(75) Zhong, L.; Li, S. Unconventional Oxygen Reduction Reaction Mechanism and Scaling Relation on Single-Atom Catalysts. *ACS Catal.* **2020**, *10* (7), 4313–4318.
(76) Copéret, C.; Chabanas, M.; Petroff Saint-Arroman, R.; Basset, J. M. Surface Organometallic Chemistry: Homogeneous and Heterogeneous Catalysis: Bridging the Gap through Surface Organometallic Chemistry. *Angew. Chem., Int. Ed.* **2003**, 156–181.
(77) Zhong, L.; Li, S. Unconventional Oxygen Reduction Reaction Mechanism and Scaling Relation on Single-Atom Catalysts. *ACS Catal.* **2020**, *10* (7), 4313–4318.
(78) Cipriano, L. A.; Di Liberto, G.; Pacchioni, G. Superoxo and Peroxo Complexes on Single-Atom Catalysts: Impact on the Oxygen Evolution Reaction. *ACS Catal.* **2022**, 11682–11691.
(79) MINGOS, D. M. P. Geometries of Dioxygen (O_2), Superoxo (O_2-) and Peroxo (O_2^{2-}) Complexes. *Nat. Phys. Sci.* **1971**, *230* (15), 154–156.
(80) Unno, M.; Chen, H.; Kusama, S.; Shaik, S.; Ikeda-Saito, M. Structural Characterization of the Fleeting Ferric Peroxo Species in Myoglobin: Experiment and Theory. *J. Am. Chem. Soc.* **2007**, *129* (44), 13394–13395.
(81) Exner, K. S.; Over, H. Kinetics of Electrocatalytic Reactions from First-Principles: A Critical Comparison with the Ab Initio Thermodynamics Approach. *Acc. Chem. Res.* **2017**, *50* (5), 1240–1247.
(82) Rebarchik, M.; Bhandari, S.; Kropp, T.; Mavrikakis, M. Insights into the Oxygen Evolution Reaction on Graphene-Based Single-Atom Catalysts from First-Principles-Informed Microkinetic Modeling. *ACS Catal.* **2023**, *13* (8), 5225–5235.
(83) Parsons, R. General Equations for the Kinetics of Electrode Processes. *Trans. Faraday Society* **1951**, *47*, 1332.
(84) Rebarchik, M.; Bhandari, S.; Kropp, T.; Mavrikakis, M. Insights into the Oxygen Evolution Reaction on Graphene-Based Single-Atom Catalysts from First-Principles-Informed Microkinetic Modeling. *ACS Catal.* **2023**, *13* (8), 5225–5235.
(85) Rossmeisl, J.; Karlberg, G. S.; Jaramillo, T.; Nørskov, J. K. Steady State Oxygenreduction and Cyclic Voltammetry. *Faraday Discuss.* **2009**, *140*, 337–346.
(86) Skubic, L.; Kopač, D.; Likozar, B.; Huš, M. Microkinetic Modelling of Heterogeneous Catalysis Revisited: Adsorption Energies Can Triumph over Activation Barriers. *Appl. Surf. Sci.* **2022**, *601*, No. 154135.
(87) Huang, Y.; Nielsen, R. J.; Goddard, W. A. Reaction Mechanism for the Hydrogen Evolution Reaction on the Basal Plane Sulfur Vacancy Site of MoS 2 Using Grand Canonical Potential Kinetics. *J. Am. Chem. Soc.* **2018**, *140* (48), 16773–16782.
(88) Sundararaman, R.; Goddard, W. A.; Arias, T. A. Grand Canonical Electronic Density-Functional Theory: Algorithms and Applications to Electrochemistry. *J. Chem. Phys.* **2017**, *146* (11), No. 114104.
(89) Baz, A.; Dix, S. T.; Holewinski, A.; Linic, S. Microkinetic Modeling in Electrocatalysis: Applications, Limitations, and Recommendations for Reliable Mechanistic Insights. *J. Catal.* **2021**, *404*, 864–872.
(90) Shinagawa, T.; Garcia-Esparza, A. T.; Takanabe, K. Insight on Tafel Slopes from a Microkinetic Analysis of Aqueous Electrocatalysis for Energy Conversion. *Sci. Rep.* **2015**, *5*, 13801.
(91) Rihm, S. D.; Akroyd, J.; Kraft, M. Modelling a Detailed Kinetic Mechanism for Electrocatalytic Reduction of CO_2. *Proc. Combust. Inst.* **2023**, *39* (4), 5647–5655.
(92) Ulissi, Z. W.; Medford, A. J.; Bligaard, T.; Nørskov, J. K. To Address Surface Reaction Network Complexity Using Scaling Relations Machine Learning and DFT Calculations. *Nat. Commun.* **2017**, *8* (1), 14621.
(93) Sutton, J. E.; Vlachos, D. G. Building Large Microkinetic Models with First-Principles′ Accuracy at Reduced Computational Cost. *Chem. Eng. Sci.* **2015**, *121*, 190–199.
(94) Maestri, M.; Vlachos, D.; Beretta, A.; Groppi, G.; Tronconi, E. Steam and Dry Reforming of Methane on Rh: Microkinetic Analysis and Hierarchy of Kinetic Models. *J. Catal.* **2008**, *259* (2), 211–222.
(95) Bramley, G. A.; Nguyen, M.-T.; Glezakou, V.-A.; Rousseau, R.; Skylaris, C.-K. Understanding Adsorption of Organics on Pt(111) in the Aqueous Phase: Insights from DFT Based Implicit Solvent and Statistical Thermodynamics Models. *J. Chem. Theory Comput.* **2022**, *18* (3), 1849–1861.
(96) Mennucci, B. Polarizable Continuum Model. *WIREs Comput. Mol. Sci.* **2012**, *2* (3), 386–404.
(97) Mennucci, B.; Tomasi, J. Continuum Solvation Models: A New Approach to the Problem of Solute's Charge Distribution and Cavity Boundaries. *J. Chem. Phys.* **1997**, *106* (12), 5151–5158.
(98) Liu, L.-M.; Zhang, C.; Thornton, G.; Michaelides, A. Reply to "Comment on `Structure and Dynamics of Liquid Water on Rutile TiO_2 (110)' " *Phys. Rev. B* **2012**, *85* (16), No. 167402.

https://doi.org/10.1021/acscatal.5c08565
ACS Catal. 2026, 16, 9810–9822

(99) Liu, L.-M.; Zhang, C.; Thornton, G.; Michaelides, A. Structure and Dynamics of Liquid Water on Rutile TiO2(110). *Phys. Rev. B* **2010**, *82* (16), No. 161415.
(100) Monteiro, M. C. O.; Dattila, F.; Hagedoorn, B.; García-Muelas, R.; López, N.; Koper, M. T. M. Absence of CO_2 Electroreduction on Copper, Gold and Silver Electrodes without Metal Cations in Solution. *Nat. Catal.* **2021**, *4* (8), 654–662.
(101) Monteiro, M. C. O.; Dattila, F.; López, N.; Koper, M. T. M. The Role of Cation Acidity on the Competition between Hydrogen Evolution and CO_2 Reduction on Gold Electrodes. *J. Am. Chem. Soc.* **2022**, *144* (4), 1589–1602.
(102) Calle-Vallejo, F.; F.de Morais R., R.; Illas, F.; Loffreda, D.; Sautet, P. Affordable Estimation of Solvation Contributions to the Adsorption Energies of Oxygenates on Metal Nanoparticles. *J. Phys. Chem. C* **2019**, *123* (9), 5578–5582.
(103) Osella, S.; Goddard, W. A. CO_2 Reduction to Methane and Ethylene on a Single-Atom Catalyst: A Grand Canonical Quantum Mechanics Study. *J. Am. Chem. Soc.* **2023**, *145* (39), 21319–21329.
(104) Cui, X.; Li, W.; Ryabchuk, P.; Junge, K.; Beller, M. Bridging Homogeneous and Heterogeneous Catalysis by Heterogeneous Single-Metal-Site Catalysts. *Nat. Catal.* **2018**, *1* (6), 385–397.
(105) Yang, X. F.; Wang, A.; Qiao, B.; Li, J.; Liu, J.; Zhang, T. Single-Atom Catalysts: A New Frontier in Heterogeneous Catalysis. *Acc. Chem. Res.* **2013**, *46* (8), 1740–1748.
(106) Misra, D.; Di Liberto, G.; Pacchioni, G. CO_2 Electroreduction on Single Atom Catalysts: Is Water Just a Solvent? *J. Catal.* **2023**, *422*, 1–11.
(107) Di Liberto, G.; Pacchioni, G. Modeling Single-Atom Catalysis. *Adv. Mater.* **2023**, *35*, 46No. 2307150.
(108) Chen, W.; Xiang, Q.; Peng, T.; Song, C.; Shang, W.; Deng, T.; Wu, J. IScience Perspective Reconsidering the Benchmarking Evaluation of Catalytic Activity in Oxygen Reduction Reaction. *iScience* **2020**, *23*, No. 101532.
(109) Xu, S.; Kim, Y.; Higgins, D.; Yusuf, M.; Jaramillo, T. F.; Prinz, F. B. Building upon the Koutecky-Levich Equation for Evaluation of Next-Generation Oxygen Reduction Reaction Catalysts. *Electrochim. Acta* **2017**, *255*, 99–108.
(110) Zana, A.; Wiberg, G. K. H.; Deng, Y. J.; Østergaard, T.; Rossmeisl, J.; Arenz, M. Accessing the Inaccessible: Analyzing the Oxygen Reduction Reaction in the Diffusion Limit. *ACS Appl. Mater. Interfaces* **2017**, *9* (44), 38176–38180.
(111) Motagamwala, A. H.; Dumesic, J. A. Microkinetic Modeling: A Tool for Rational Catalyst Design. *Chem. Rev.* **2021**, 1049–1076.
(112) Sanville, E.; Kenny, S. D.; Smith, R.; Henkelman, G. Improved Grid-Based Algorithm for Bader Charge Allocation. *J. Comput. Chem.* **2007**, *28* (5), 899–908.
(113) Tang, W.; Sanville, E.; Henkelman, G. A Grid-Based Bader Analysis Algorithm without Lattice Bias. *J. Phys.: Condens. Matter* **2009**, *21* (8), No. 084204.
(114) Henkelman, G.; Arnaldsson, A.; Jónsson, H. A Fast and Robust Algorithm for Bader Decomposition of Charge Density. *Comput. Mater. Sci.* **2006**, *36* (3), 354–360.
(115) Bader, R. F. W. Atoms in Molecules. *Acc. Chem. Res.* **1985**, *18* (1), 9–15.
(116) Singh, B.; Gawande, M. B.; Kute, A. D.; Varma, R. S.; Fornasiero, P.; McNeice, P.; Jagadeesh, R. V.; Beller, M.; Zbořil, R. Single-Atom (Iron-Based) Catalysts: Synthesis and Applications. *Chem. Rev.* **2021**, *121* (21), 13620–13697.
(117) Liu, X.; Dai, L. Carbon-Based Metal-Free Catalysts. *Nat. Rev. Mater.* **2016**, *1* (11), 16064.
(118) Gawande, M. B.; Fornasiero, P.; Zbořil, R. Carbon-Based Single-Atom Catalysts for Advanced Applications. *ACS Catal.* **2020**, *10* (3), 2231–2259.

https://doi.org/10.1021/acscatal.5c08565
ACS Catal. 2026, 16, 9810−9822